Journal of Magnetic Resonance 208 (2011) 298–304

Contents lists available at ScienceDirect

Journal of Magnetic Resonance

journal homepage: www.elsevier.com/locate/jmr

Communication

Interdependence of in-cell xenon density and temperature during Rb/^{129}Xe spin-exchange optical pumping using VHG-narrowed laser diode arrays

Nicholas Whiting [a,1], Panayiotis Nikolaou [a], Neil A. Eschmann [a,2], Boyd M. Goodson [a,*], Michael J. Barlow [b]

[a] Department of Chemistry and Biochemistry, Southern Illinois University, Carbondale IL 62901, United States
[b] Sir Peter Mansfield Magnetic Resonance Centre, University of Nottingham, Nottingham, NG7 2RD, UK

ARTICLE INFO

Article history:
Received 4 October 2010
Revised 23 November 2010
Available online 2 December 2010

Keywords:
Spin-exchange optical pumping
Hyperpolarization
Xenon NMR/MRI
Low-field NMR
Laser diode array

ABSTRACT

The ^{129}Xe nuclear spin polarization (P_{Xe}) that can be achieved via spin-exchange optical pumping (SEOP) is typically limited at high in-cell xenon densities ($[Xe]_{cell}$), due primarily to corresponding reductions in the alkali metal electron spin polarization (e.g. P_{Rb}) caused by increased non-spin-conserving Rb–Xe collisions. While demonstrating the utility of volume holographic grating (VHG)-narrowed lasers for Rb/^{129}Xe SEOP, we recently reported [P. Nikolaou et al., JMR 197 (2009) 249] an anomalous dependence of the observed P_{Xe} on the in-cell xenon partial pressure (p_{Xe}), wherein P_{Xe} values were abnormally low at decreased p_{Xe}, peaked at moderate p_{Xe} (~300 torr), and remained surprisingly elevated at relatively high p_{Xe} values (>1000 torr). Using *in situ* low-field ^{129}Xe NMR, it is shown that the above effects result from an unexpected, inverse relationship between the xenon partial pressure and the optimal cell temperature (T_{OPT}) for Rb/^{129}Xe SEOP. This interdependence appears to result directly from changes in the efficiency of one or more components of the Rb/^{129}Xe SEOP process, and can be exploited to achieve improved P_{Xe} with relatively high xenon densities measured at high field (including averaged P_{Xe} values of ~52%, ~31%, ~22%, and ~11% at 50, 300, 500, and 2000 torr, respectively).

© 2010 Elsevier Inc. All rights reserved.

1. Introduction

The high nuclear spin polarization of hyperpolarized (HP) noble gases (e.g. ^{129}Xe, ^{83}Kr, and ^{3}He) can be exploited to increase NMR detection sensitivity by several orders of magnitude, leading to their use in a variety of magnetic resonance applications [1,2], including: biomedical MR imaging and spectroscopy [3–8]; probing pores and surfaces of molecules and materials [9–17]; xenon biosensors [18,19]; and low-field [20,21] and remotely-detected [22] NMR and MRI—as well as experiments where HP gases are employed as nuclear magnetization *sources* for other species [23–26]. HP gases are commonly produced via spin-exchange optical pumping (SEOP) [27–30]. SEOP is a two-step process whereby angular momentum is transferred from resonant, circularly-polarized (CP) light to the electronic spins of an alkali metal vapor (e.g. Rb), and is then subsequently transferred to the nuclear spins of the noble gas during collisions.

The efficiency of SEOP depends on the identities of the noble gas and alkali metal species involved, as well as the conditions within the OP cell [27]. Consider the specific example of Rb/^{129}Xe SEOP. Achieving high (>10%) ^{129}Xe nuclear spin polarization (P_{Xe}) values typically requires low in-cell xenon density ($[Xe]_{cell}$) during SEOP—mostly because xenon itself limits the achievable rubidium electron spin polarization (P_{Rb}) through non-spin-conserving Rb–Xe collisions [30–32]. Moreover, Rb–Xe spin exchange is expected to become increasingly inefficient at high xenon (and total gas) cell densities [29] (particularly as the Xe partial pressure, p_{Xe}, exceeds much more than a few tens of torr). Because of these effects, increases in $[Xe]_{cell}$ are compensated by corresponding losses in P_{Xe}; for example, the NMR 'signal-to-concentration ratio' (SCR) is generally expected to exhibit a flat (or worse) dependence upon increasing $[Xe]_{cell}$ (e.g. [32]). Correspondingly, impressive demonstrations of very high (>50%) P_{Xe} values have generally depended not only on innovative designs and technological developments, but also on limiting the xenon partial pressure in the cell (often $\leqslant$30 torr at loading) [33–38]. The desire to maintain low $[Xe]_{cell}$ complicates the production of large amounts of HP ^{129}Xe with high polarization (required for many of the aforementioned NMR/MRI applications); indeed, most current implementations employ complex (and often expensive) set-ups that polarize a small amount of Xe at an instant and cryogenically accumulate the HP gas over time [30,34–38].

While demonstrating the utility of volume holographic grating (VHG)-narrowed lasers for Rb/^{129}Xe SEOP, we recently reported an anomalous dependence of the observed P_{Xe} on $[Xe]_{cell}$, wherein

* Corresponding author. Fax: +1 618 453 6408.
E-mail address: bgoodson@chem.siu.edu (B.M. Goodson).
[1] Present address: Sir Peter Mansfield Magnetic Resonance Centre, University of Nottingham, UK.
[2] NSF REU student; affiliation when this research was performed: Southwestern Illinois College, Belleville, IL. Present address: Department of Chemistry, University of California Santa Barbara.

1090-7807/$ - see front matter © 2010 Elsevier Inc. All rights reserved.
doi:10.1016/j.jmr.2010.11.016

P_{Xe} values were abnormally low at decreased $[Xe]_{cell}$, peaked at moderate $[Xe]_{cell}$ ($p_{Xe} \sim 300$ torr), and remained surprisingly elevated at relatively high $[Xe]_{cell}$ values ($p_{Xe} > 1000$ torr) [39]. Using *in situ* low-field ^{129}Xe NMR, it is shown that such effects result from an unexpected, inverse relationship between the xenon partial pressure within the cell and the optimal cell temperature (T_{OPT}) for Rb/^{129}Xe SEOP. This interdependence appears to result directly from changes in the efficiency of one or more components of the Rb/^{129}Xe SEOP process (and not, say, to some temperature- or Xe-density-dependent change to ^{129}Xe spin-relaxation rates). This effect can be exploited to achieve improved P_{Xe} with relatively high xenon densities in the cell.

2. Background

In Rb/^{129}Xe SEOP [27–30], the maximum ^{129}Xe nuclear spin polarization attainable is limited by the volume-averaged Rb electron polarization:

$$\langle P_{Rb}(z,r)\rangle = \frac{\gamma_{OP}(z,r)}{\gamma_{OP}(z,r)+\Gamma_{SD}}, \tag{2.1}$$

where (z,r) specifies the 'depth' into a cylindrical cell (z) and the radial distance (r) from the cell's central axis, and $\gamma_{OP}(z,r)$ is the position-dependent OP rate within the cell, given by [40]:

$$\gamma_{OP}(z,r) = \int \Phi(z,r,\nu)\cdot\sigma_0(\nu)d\nu, \tag{2.2}$$

where $\Phi(z,r,\nu)$ is the light flux per unit frequency (ν) at position (z,r) and $\sigma_0(\nu)$ is the Rb D_1 absorption cross-section. In Eq. (2.1), Γ_{SD} is the Rb electron spin destruction (SD) rate, which (away from the cell walls) is given by:

$$\Gamma_{SD} = \sum_i \kappa_{SD}^i \cdot [M_i], \tag{2.3}$$

where κ_{SD}^i is the SD rate per collision with a given gas species (i) and $[M_i]$ is its number density; κ_{SD} values of 2×10^{-18}, 9×10^{-18}, and 5.2×10^{-15} cm^3 s^{-1} have been measured for He, N_2, and Xe, respectively [30–32]. Thus even at low $[Xe]_{cell}$, the SD rate from Rb/Xe collisions generally dwarfs the contributions from other gases—lowering the achievable values for both P_{Rb} and P_{Xe}.

Although the Rb density is orders of magnitude lower than that of Xe—and the chance of a mutual spin-flip during an encounter is low [27]—P_{Xe} may accumulate over time [40]:

$$P_{Xe} = \langle P_{Rb}\rangle \cdot \left(\frac{\gamma_{SE}}{\gamma_{SE}+\Gamma_{Xe}}\right)\cdot\{1-\exp[-(\gamma_{SE}+\Gamma_{Xe})t]\}, \tag{2.4}$$

where γ_{SE} is the Rb–Xe spin-exchange (SE) rate and Γ_{Xe} is the ^{129}Xe nuclear spin destruction rate (or, $1/T_1^{Xe}$). During SEOP, the primary contributors to Γ_{Xe} will generally be wall collisions (diffusion through local field gradients and gas-phase collisions with other species are expected to provide much weaker contributions [41,42]). The Rb–Xe spin-exchange is mediated by two-body collisions and three-body complex formations (typically Rb–Xe–N_2 or Rb–Xe–Xe [29]). The efficiency of the Rb–Xe polarization transfer is determined by γ_{SE}, given by [29,30,32]:

$$\gamma_{SE} = [Rb]_{cell}\cdot\left\{\frac{\gamma_{RbXe}}{[Xe]_{cell}}\left(\frac{1}{1+br}\right)+\langle\sigma v\rangle\right\}, \tag{2.5}$$

where $[Rb]_{cell}$ is the Rb number density (typically $\sim10^{11}$–10^{14}/cm^3, dependent upon T_{cell}) [27], γ_{RbXe} is the 3-body SE rate, $\langle\sigma v\rangle$ is the velocity-averaged 2-body SE cross-section (in cm^3/s), and $(1+br)^{-1}$ is a factor that takes into account the use of a binary Xe/N_2 gas mixture, where $br = (0.275)\cdot(N_2\text{ pressure})\cdot(\text{Xe pressure})^{-1}$ [28,29] (here N_2 is added to quench unwanted Rb fluorescence [30,43] and to collision-broaden the Rb absorption line [27,44]). The proficiency of spin-exchange under a particular set of conditions can be monitored via the time constant of the P_{Xe} build-up curves (Γ) [29]:

$$\begin{aligned}\Gamma &= [Rb]_{cell}\cdot\left\{\frac{\gamma_{RbXe}}{[Xe]_{cell}}\left(\frac{1}{1+br}\right)+\langle\sigma v\rangle\right\}+\Gamma_{Xe}\\ &= [Rb]_{cell}\cdot\gamma'+\Gamma_{Xe},\end{aligned} \tag{2.6}$$

where γ' comprises both 2-body and 3-body contributions to γ_{SE} (i.e. $\gamma_{SE} = \gamma'\cdot[Rb]_{cell}$), and in principle can be determined from the slope of a linear plot of Γ versus $[Rb]_{cell}$ (with Γ_{Xe} as the y-intercept) [29]. Similarly, systematic measurements of γ' values and Eq. (2.6) should in principle allow discrimination of the respective contributions from 2-body and 3-body interactions to the overall spin-exchange rate using [29]:

$$\gamma' = \left\{\frac{\gamma_{RbXe}}{2.48\times10^{19}\text{ cm}^{-3}}\left(\frac{1}{P_a}\right)+\langle\sigma v\rangle\right\}, \tag{2.7}$$

where 2.48×10^{19} cm^{-3} is the number density of 760 torr Xe gas at 296 K, and P_a^{-1} is a dimensionless quantity given by [29]:

$$\left(\frac{1}{P_a}\right) = \left\{\frac{760\text{ torr}}{p_{Xe}}\right\}\cdot\left(\frac{1}{1+br}\right). \tag{2.8}$$

A plot of γ' versus P_a^{-1} should result in a straight line; from the slope, one can calculate the rate γ_{RbXe} (using Eq. (2.7)), with the y-intercept providing the 2-body term ($\langle\sigma v\rangle$). The 2-body term should exceed the 3-body contribution with Xe pressures greater than a few hundred torr [29].

Finally, P_{Xe} will accumulate over time—reaching steady-state (from Eq. (2.4)) [40]:

$$P_{Xe}(t=\infty) = \frac{\gamma_{SE}}{\gamma_{SE}+\Gamma_{Xe}}\cdot\langle P_{Rb}(z,r)\rangle. \tag{2.9}$$

Thus, the steady-state P_{Xe} is limited by the volume-averaged Rb polarization $\langle P_{Rb}(z,r)\rangle$, along with the relative magnitudes of γ_{SE} and Γ_{Xe}.

3. Results and discussion

3.1. Dependence of optimal temperature for SEOP (T_{OPT}) on xenon partial pressure

The dependence of the ^{129}Xe polarization efficiency on the gas composition and cell temperature was monitored *in situ* via low-field NMR. For example, Fig. 1a shows the NMR signal from HP ^{129}Xe gas within the OP cell as a function of T_{cell} for different cell loadings where the xenon partial pressure was varied, but the total cell pressure at loading was held constant (each point was taken following 5 min. of SEOP). The temperature at which the peak ^{129}Xe NMR signal was achieved was observed to depend sensitively upon p_{Xe}: The optimal temperature (T_{OPT}) for SEOP was relatively high for the lowest Xe partial pressure studied (50 torr), but was observed to follow a qualitatively inverse relationship with p_{Xe}, shifting smoothly to lower temperatures with increasing Xe partial pressure (see Fig. 1a *inset*). Additionally, the increase in signal with Xe partial pressure indicates that the loss in P_{Xe} is more gradual than the increase in $[Xe]_{cell}$. Indeed, upon division of the low-field ^{129}Xe NMR signal in Fig. 1a by p_{Xe} (to obtain a relative estimate of ^{129}Xe polarization), we observed that P_{Xe} is higher at lower p_{Xe} (as expected)—but only near T_{OPT}, and not to the degree that would maintain a constant SCR upon increased $[Xe]_{cell}$; on the other hand, at lower cell temperatures P_{Xe} peaks at moderate Xe partial pressures (Fig. 1b) [45], in qualitative agreement with Ref. [39].

The above behavior may be compared with that observed upon varying the in-cell nitrogen partial pressure (p_{N2}), with the Xe partial pressure held constant at 300 torr (Fig. 1c). While a small

increase in ^{129}Xe NMR signal was observed with higher total cell pressures[3], T_{OPT} was poorly sensitive to changes in p_{N2} (see Fig. 1c *inset*). Similar experiments using a tertiary gas mixture (Xe, N_2, and He) also exhibited little variation in T_{OPT}, signaling that this optimal temperature effect is most likely due to changes in p_{Xe} itself, and not some other aspect of gas composition or density.

3.2. Studies of SEOP efficiency as a function of T_{cell} and xenon partial pressure

While partially explaining our previously reported results [39] regarding the uncharacteristically high P_{Xe} values at high p_{Xe} (as well as low P_{Xe} at low p_{Xe}—note that all data in Ref. [39] were taken at $T_{cell} = 80$ °C, favoring SEOP performance at higher p_{Xe} values according to present data), time-dependent studies of SEOP dynamics were performed to gain additional insight into the interplay of T_{OPT} and p_{Xe}. Although P_{Rb} reaches steady-state with the local photon flux within a fraction of a second [27], the accumulation of spin polarization in the ^{129}Xe nuclei is a much slower process—and can be monitored *in situ* at low field.

The selected ^{129}Xe NMR time courses in Fig. 2 provide an indication of how the xenon polarization dynamics can change non-trivially under two different circumstances: variable p_{Xe} but constant T_{cell} (90 °C, Fig. 2a); and variable T_{cell} but constant p_{Xe} (500 torr Xe, Fig. 2b). The P_{Xe} build-up curves were fit to $S(t) = a \cdot [1 - \exp(-\Gamma t)]$ (c.f. Eq. (2.4)), thus parameterizing each fit by two values: Γ (the overall rate constant for P_{Xe} build-up—equal to $\gamma_{SE} + \Gamma_{Xe}$); and a, the steady-state ^{129}Xe NMR signal ($=\xi[Xe]_{cell} \cdot \langle P_{Rb}\rangle \cdot \gamma_{SE} \cdot \Gamma^{-1}$, where ξ is an instrument function). Contrary to expectations, runs in Fig. 2a with higher p_{Xe} loadings exhibited greater P_{Xe} build-up rates (higher $[Xe]_{cell}$ is expected to both decrease γ_{SE} and increase Γ_{SD}); note that these runs were performed at a common (low) temperature, shown in Fig. 1 to favor SEOP at higher Xe densities under our conditions. Correspondingly, these curves also exhibit increasing steady-state ^{129}Xe NMR signal with increasing Xe partial pressure (indicating that the fall-off in P_{Xe} is much slower than the anticipated rise in Rb spin destruction from increasing $[Xe]_{cell}$).

The P_{Xe} accumulation rate would be expected to rise steeply with cell temperature (due to rapidly increasing $[Rb]_{cell}$, which has a proportional relationship with γ_{SE}), and indeed this is observed in the fixed-p_{Xe} curves (Fig. 2b). However, this set of curves also demonstrates the utility of optical pumping at T_{OPT}, as the highest steady-state ^{129}Xe signals were achieved at the optimal cell temperature for this Xe loading (85 °C for 500 torr Xe). More generally, larger γ_{SE} values should translate to higher P_{Xe} values—to a point: once the Rb density grows too high, poor illumination of the rear and outer portions of the cell volume will cause the overall $\langle P_{Rb}\rangle$ to fall [34,46] (as 'dark' Rb is essentially unpolarized)—capping the value of P_{Xe} that can be achieved. Moreover, at the highest temperatures (e.g. $\geqslant$110 °C), the strong light absorption caused by the high Rb density (and likely, lower $\langle P_{Rb}\rangle$) can lead to instabilities associated with "rubidium runaway" [34], as increased light absorption heats up the cell—vaporizing more Rb, increasing the cell opacity, and decreasing $\langle P_{Rb}\rangle$ in a self-reinforcing way.

Although there are weak $[Xe]_{cell}$-dependent contributions to gas-phase Xe T_1 processes [41,42], significant variation in Γ_{Xe} values would be unexpected under the range of conditions explored here. Nevertheless, multiplication of the parameters (a and Γ) extracted from the P_{Xe} accumulation curves and division by $[Xe]_{cell}$ should give a number proportional to $\langle P_{Rb}\rangle \cdot \gamma_{SE}$,

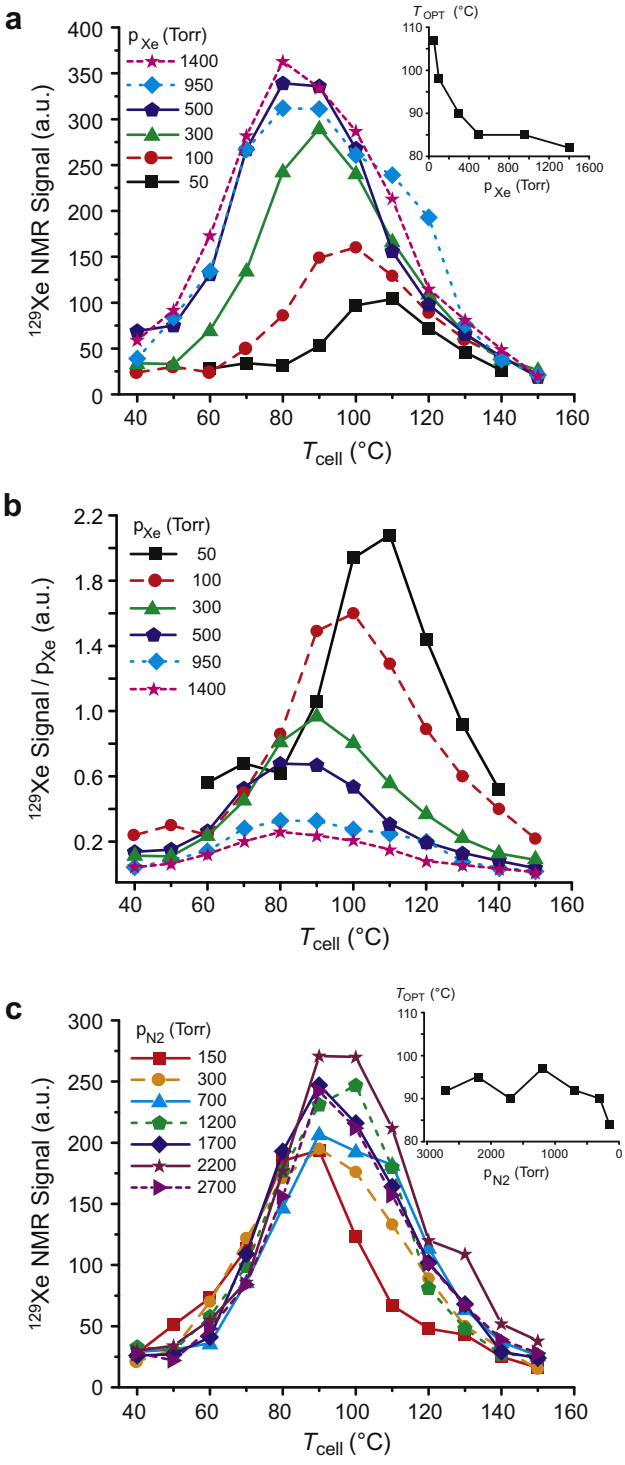

Fig. 1. (Color online) (a) *In situ* low-field NMR signal from HP ^{129}Xe gas as a function of the cell exhaust temperature (T_{cell}) for various p_{Xe}. For all experiments, the cell was back-filled with N_2 to give a total pressure of ~2000 torr; OP time was 5 min. *Inset:* dependence of the optimal temperature for OP (T_{OPT}) on p_{Xe}, as estimated from the data in the main figure. (b) Same as (a), but with the low-field ^{129}Xe NMR signal divided by p_{Xe}, to provide relative polarization enhancements. (c) Same as (a), but for various p_{N2} (for these runs, p_{Xe} was held at 300 torr). *Inset:* Dependence of T_{OPT} on p_{N2} for corresponding OP runs, showing little discernable dependence (on either p_{N2} or overall cell pressure). (For interpretation of the references to color in this figure legend, the reader is referred to the web version of this article.)

[3] This observation was likely due simply to increased collision-broadening of the Rb D_1 line as the total cell pressure was increased; transmitted laser spectra show additional light absorption at higher cell pressures. Note that 150 torr of N_2 (the lowest amount utilized) should be sufficient to quench Rb fluorescence and radiation trapping. Any other contributions (e.g., from possible deviations from the current modeling of pressure-dependent three-body contributions to Rb-Xe spin exchange) would likely be overshadowed by the pressure-dependent changes to the Rb absorption profile.

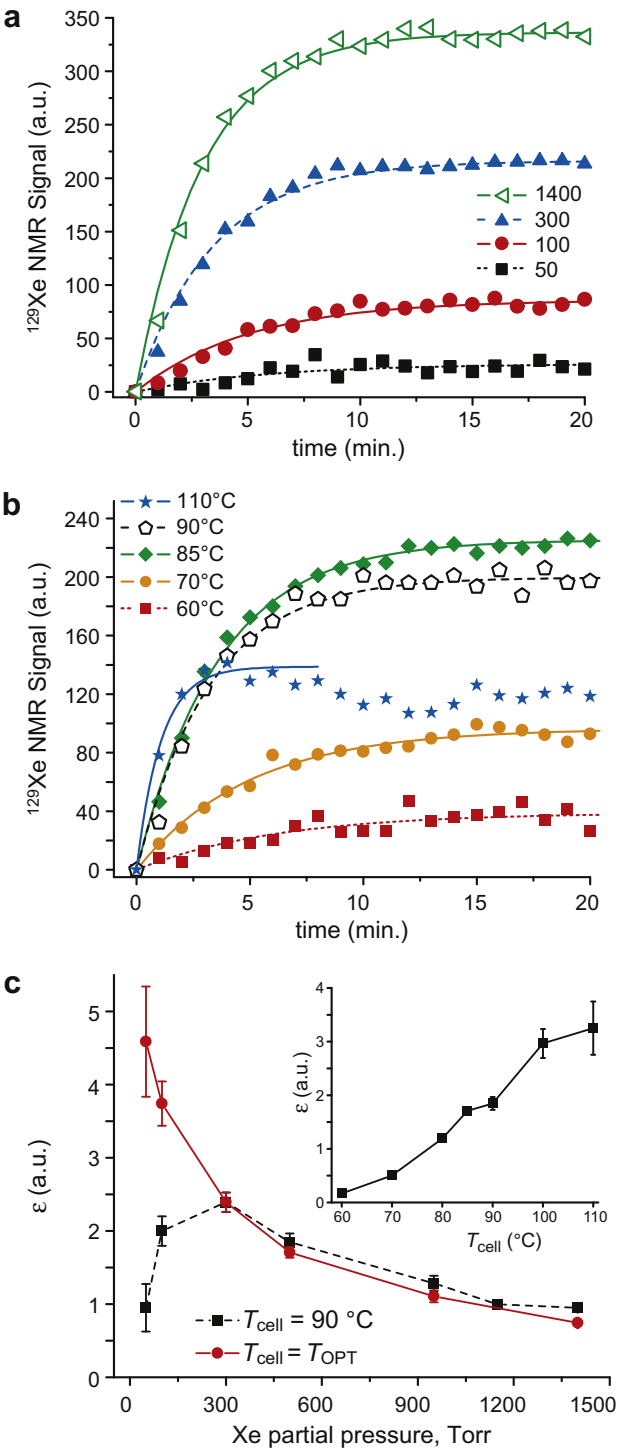

Fig. 2. (Color online) (a) Selected curves showing the time dependence of the *in situ* low-field HP ^{129}Xe NMR signal during SEOP, shown for various p_{Xe} (T_{cell} = 90 °C). Each dataset is the average of four runs; solid lines are exponential fits as described in the text. (b) Same as (a), but with variable T_{cell} and fixed p_{Xe} (500 torr). Curve fits were truncated at the highest T_{cell} values ($\geqslant$110 °C), due to instabilities likely caused by 'rubidium runaway' effects [34]. (c) Plots of Γ multiplied by the steady-state value of the low-field NMR signal (a), and divided by $[Xe]_{cell}$ (using the factor: 760 torr/Xe partial pressure, to adjust for the variation in ^{129}Xe spin density) giving: $\varepsilon = \xi \cdot \langle P_{Rb} \rangle \cdot \gamma_{SE}$, where ξ is an instrument function. Data points are plotted as functions of p_{Xe}. Black squares/dotted line: data points obtained at fixed T_{cell} = 90 °C; Red circles/solid line: data points obtained at $T_{cell} = T_{OPT}$. *Inset:* Same as main figure, except plotted versus T_{cell} for fixed p_{Xe} (500 torr Xe). Error bars are fit uncertainties. For all experiments, the cell was back-filled with N_2 after Xe loading to give a constant 2000 torr total pressure. (For interpretation of the references to color in this figure legend, the reader is referred to the web version of this article.)

represented here by the symbol ε; thus ε essentially provides a Xe density-normalized figure of merit for SEOP efficiency that is free of contributions from the ^{129}Xe nuclear spin-relaxation rate (Fig. 2c). When performing SEOP at a constant T_{cell} (90 °C), ε initially rises with increasing p_{Xe}, peaks, and then slowly falls off at high Xe densities; this trend qualitatively follows the previously reported, unexpected dependence of P_{Xe} on p_{Xe} at high Xe densities [39]. However, when SEOP is performed at each p_{Xe}'s optimal temperature (T_{OPT}), high SEOP efficiency is observed at low p_{Xe}, dropping off smoothly and dramatically with increased Xe density (i.e. exhibiting the traditionally expected dependence). As an aside, we note that T_{OPT} is not necessarily where the SEOP efficiency (at least, as represented by $\varepsilon \propto \gamma_{SE} \cdot \langle P_{Rb} \rangle$) is the highest (Fig. 2c *inset*): Here, T_{OPT} is the temperature at which the steady-state P_{Xe} is maximized. But particularly at high temperatures, $\gamma_{SE} \gg \Gamma_{Xe}$, causing $P_{Xe}(t = \infty) \to \langle P_{Rb} \rangle$ according to Eq. (2.9); thus, even under conditions where γ_{SE} is very high (giving rise to steadily increasing ε values), $\langle P_{Rb} \rangle$—and by extension P_{Xe}—can still suffer from poor cell illumination. In any case, because the factor ε is devoid of contributions from Γ_{Xe}, the results in Fig. 2c indicate that the interdependence of p_{Xe} and T_{cell} that determines P_{Xe} is due to some facet of the SEOP process itself (and not, say, to temperature- or density-dependent changes to ^{129}Xe spin relaxation).

In principle, the data from the P_{Xe} build-up curves can be further analyzed to determine the 2-body and 3-body contributions to Rb/^{129}Xe spin-exchange and the intrinsic P_{Xe} relaxation. By plotting Γ as a function of $[Rb]_{cell}$ (here, estimated from literature vapor–pressure curves [47]), one should obtain a straight line with a slope equal to γ' (the overall SE cross-section) and a y-intercept equal to Γ_{Xe} (Eq. (2.6)). As shown in Fig. 3a, using this approach with the variable-temperature data (500 torr, Fig. 2b) yields a good linear fit with $\gamma' = 1.2 \times 10^{-15}$ cm^3 s^{-1} (with fit error of $\pm 4 \times 10^{-17}$ cm^3 s^{-1}); this value appears to be a reasonable estimate, with previous measures typically ranging between $\sim 9 \times 10^{-15}$ and $\sim 8 \times 10^{-17}$ cm^3 s^{-1} (depending on gas mixture and technique—see, e.g. Refs. [27,29,48]). From this fit, Γ_{Xe} was found to be $\sim$0.0017 s^{-1}, corresponding to an in-cell ^{129}Xe T_1 of $\sim$10 min. In principle, repeating the process of determining γ' for multiple $[Xe]_{cell}$ values should allow the 2-body and 3-body contributions to the spin-exchange rate to be distinguished: Plotting γ' as a function of $1/P_a$ (see Eqs. (2.7) and (2.8)) is expected [29] to result in a straight line with a slightly increasing slope; one could extract values for the 2-body (y-intercept) and 3-body (slope) contributions from a linear fit of such data. Although our data is limited (see caption), we attempted to replicate this approach to extract the 2-body and 3-body contributions to γ'; however, the expected dependence was not observed (hindering these efforts). More specifically, the data appear not only to show overall higher-than-expected values (at least compared to previous measurements of the binary SE cross-section (e.g. $\langle \sigma v \rangle \sim 3.7 \times 10^{-16}$ cm^3 s^{-1} from Ref. [29]), but also appear to show higher γ' values at higher Xe densities—counter to expectation (as $1/P_a$ is inversely proportional to p_{Xe}). While the higher-than-expected nature of our γ' values could reflect the reliance on vapor–pressure curves to estimate $[Rb]_{cell}$[4], the origin of the unexpected trend is unclear (but the behavior does appear to be consistent with our overall findings of high P_{Xe} values at high xenon densities).

[4] For example, laser-heating of the cell (not sufficiently reflected in the measurement of the temperature of the oven's exhaust air from the cell) could cause a systematic underestimate of $[Rb]_{cell}$ that may grow larger with increasing laser absorption/cell opacity (i.e., causing the error to grow with increasing 'actual' temperature).

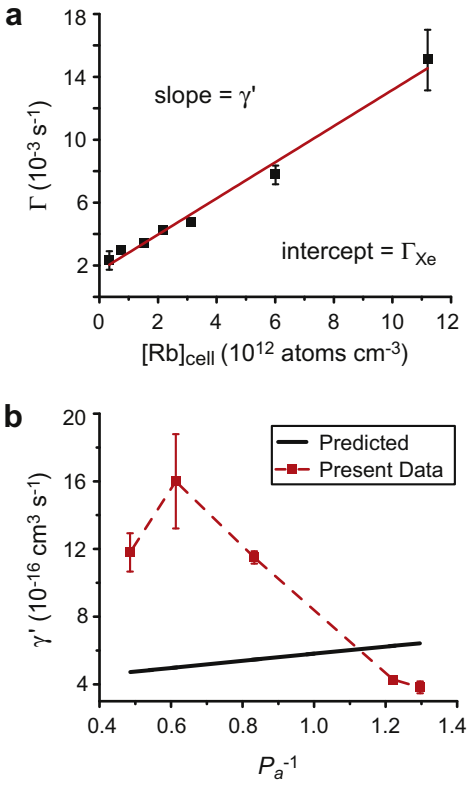

Fig. 3. (Color online) (a) Plots of the time constant for HP ^{129}Xe polarization build-up (Γ) measured at fixed p_{Xe} (500 torr Xe) versus $[Rb]_{cell}$ (estimated from vapor–pressure curves [47]). Following Ref. [29], a fit to the data (red line) should give a slope and intercept that correspond respectively to the total spin-exchange cross-section, γ' ($\sim 1.15 \times 10^{-15} \pm 4 \times 10^{-17}$ cm^3 s^{-1}) and the in-cell ^{129}Xe nuclear spin-relaxation rate, Γ_{Xe} ($\sim$0.00166 s^{-1}). (b) Plot of γ' versus $1/P_a$ (see Eqs. (2.7) and (2.8)) determined for different values of $[Xe]_{cell}$ (red dotted line); the point at $P_a^{-1} = 0.83$ (corresponding to 500 torr Xe) was taken from the fit of Γ values obtained at multiple temperatures shown in (a); all other points were obtained by fitting Γ values obtained at two temperatures and using the Γ_{Xe} from (a) as the intercept (i.e. assuming no dependence of Γ_{Xe} on $[Xe]_{cell}$). The solid line (black) is the predicted trend [29]. (For interpretation of the references to color in this figure legend, the reader is referred to the web version of this article.)

3.3. High-field measurements of P_{Xe} following SEOP with high in-cell Xe densities

The observed p_{Xe}/T_{OPT} dependence was exploited to achieve exceptionally high P_{Xe} values over a wide range of high in-cell Xe partial pressures (50–2000 torr) and only $\sim$29 W of frequency-narrowed laser power. Several series of Rb/^{129}Xe SEOP runs were performed at different temperatures with variable Xe densities, followed by gas collection and transfer to high field (9.4 T). To better illustrate the effect of the p_{Xe}/T_{OPT} interdependence on the SEOP performance, the P_{Xe} data in Fig. 4 are split into two groups according to the SEOP cell temperature: 'hot' (T_{cell} = 100–110 °C) and 'cold' (T_{cell} = 85–90 °C). Importantly, the high-field data qualitatively reproduce the trends observed in the low-field *in situ* studies (Figs. 1 and 2), with higher P_{Xe} values achieved at lower T_{cell} for higher Xe densities (and vice versa)—yielding a $\sim$2-fold difference in P_{Xe} at the highest Xe loadings. Moreover, while performing SEOP at lower temperatures resulted in somewhat lower P_{Xe} values at the lowest Xe loadings ($\leqslant$100 torr), the fall-off in P_{Xe} with increasing p_{Xe} is much more gradual under these conditions—to the point of being virtually independent of Xe partial pressure above $\sim$1000 torr. Correspondingly, we continued to observe stronger ^{129}Xe NMR signals with increasing Xe partial pressures (as shown in the figure as the product of P_{Xe} and p_{Xe}), thus surpassing the typically expected trend for the signal-to-concentration ratio with increasing $[Xe]_{cell}$. In any case, performing SEOP at or near the respective T_{OPT} values yielded average P_{Xe} values of 52% ± 6%, 40% ± 8%, 31% ± 6%, 22.3% ± 1.5%, 12.8% ± 1.1%, 11.8% ± 1.0%, and 11.0% ± 0.3% for cells loaded with 50, 100, 300, 500, 950, 1400, and 2000 torr Xe, respectively. To our knowledge, these are the highest P_{Xe} values yet reported at such high $[Xe]_{cell}$ values ($\sim$0.06 to $\sim$2.6 amagat) for Rb/^{129}Xe SEOP.

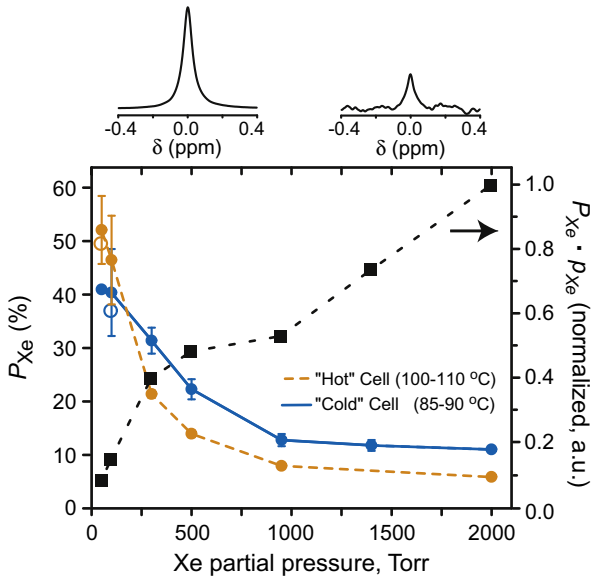

Fig. 4. (Color online) *Left axis*: measurements of P_{Xe} obtained following SEOP and subsequent transfer of HP Xe gas to high field (9.4 T) for various values of p_{Xe}. Data as shown are grouped into two different cell temperature ranges: 'Hot cell' (orange dotted line)—T_{cell} = 100–110 °C; and 'Cold cell' (blue solid line)—T_{cell} = 85–90 °C (lines are meant only to guide the eye). Values and error bars correspond to averages and standard deviations obtained for multiple (typically $\sim$2–5) SEOP runs. Open symbols correspond to additional (non-optimal) runs performed outside of the stated temperature ranges. *Right axis*: corresponding normalized HP ^{129}Xe NMR signal intensities (black dashed line; product of $P_{Xe} \cdot p_{Xe}$) for each p_{Xe} under optimal OP conditions. For all experiments, the cell was back-filled with N_2 after Xe loading to give a constant 2000 torr total pressure (exception: runs with 2000 torr Xe partial pressure contained an additional 600 torr N_2). *Top:* Examples of high-field (9.4 T) NMR spectra of HP (*left*) and thermal (*right*) ^{129}Xe for p_{Xe} = 300 torr (*left:* spectrum from one 6° pulse; *right*: averaged from 1100 acquisitions with 90° pulses; calculated enhancement: $\sim$42,900; P_{Xe} = $\sim$39%. (For interpretation of the references to color in this figure legend, the reader is referred to the web version of this article.)

4. Summary and conclusions

Using low-field *in situ* NMR studies of Rb/^{129}Xe SEOP, we have shown that a previously-reported anomalous dependence of P_{Xe} on the xenon partial pressure observed under our conditions is the result of an unexpected, inverse relationship between the xenon density and the optimal cell temperature for SEOP. This interdependence appears to result directly from changes in the efficiency of one or more components of the Rb/^{129}Xe SEOP process itself (as opposed to changes in the ^{129}Xe spin-relaxation rate). The effect was exploited to achieve the highest P_{Xe} values yet reported at such high in-cell Xe densities (to our knowledge). We anticipate that these results will be relevant to NMR/MRI applications where significant quantities of highly polarized xenon are required (as these studies may point to improved HP gas production methods with greater efficiency, experimental simplicity, or lower cost), as well as to SEOP approaches employing different experimental configurations, alkali metals, and/or noble gas isotopes. The origin of the interdependence of Xe pressure and T_{OPT} is not yet understood. While at a very preliminary stage, recent simulations have

suggested that part (but not all) of the observed effect is a consequence of the high flux and narrow bandwidth of the incident light used for SEOP. In any case, this effect—along with the respective roles of laser-offset dependence (to be studied with new tunable 'on-chip' VHG-narrowed sources [49]), buffer-gas-induced changes to the Rb absorption lineshape [44], and the effects of ultrahigh buffer gas temperatures [50] expected under our conditions—are subjects of ongoing work.

5. Methods

All Rb/^{129}Xe SEOP experiments were conducted using a 'fixed-frequency' laser diode array (LDA) production prototype [39] ('Comet'; Newport/Spectra-Physics) frequency-narrowed with integrated VHG. Nominal LDA conditions: driving current: 52 amps; laser output power (at cell): ~29 W; output linewidth: ~0.27 nm; centroid: ~794.66 nm (the laser is specifically driven to have a 'blue-side' spectral offset from the Rb D_1 line (nominally 794.76 nm) to achieve maximum P_{Xe} under these conditions [39]). The LDA is TEC-cooled and fiber-coupled into a binocular circular polarizer box (Coherent) to illuminate the OP cell (giving a ~85/15 straight/angled beam ratio). The non-LDA components of the apparatus have been described previously [43]. Briefly, the OP apparatus—centered around a Rosen cell [40] (75 cc inner cell volume) residing in a Helmholtz coil (HC) pair (22″ i.d. ~32 G)—permits operation in either batch or "stop-flow" mode and allows for arbitrary gas mixtures/densities of Xe, N_2, and He. The cell is supported and positioned with custom (non-magnetic) PTFE cell mounts and Garolite posts on translation stages. Nominal SEOP conditions: single-batch-mode OP; binary Xe/N_2 gas mixture; cell gas pressures: 50–1400 torr Xe (natural isotopic ^{129}Xe abundance), back-filled with N_2 gas to give ~2000 torr total pressure; and up to ~20 min. OP time. Since our last publication [39], a number of improvements have been implemented, including a 2″ mirror installed behind the cell to retro-reflect excess transmitted laser light back into the OP cell; this practice was found to provide up to a ~29% 'free' increase in P_{Xe} (under nominal conditions; dependent on T_{cell}) [45].

Low-field NMR detection was performed with a Magritek Aurora NMR spectrometer (^{129}Xe frequency: 37.5 kHz). Acquisition was typically performed as follows [45]: after a series of (~300–500) 'crusher' pulses to re-zero P_{Xe}, the laser is unblocked and the polarization is allowed to accumulate for a set time before a single 1.25 ms pulse (~52°) is applied via a 1.75″-wide homebuilt transmit/receive coil pair (residing over the middle quarter of the inner cell volume) to measure the ^{129}Xe NMR signal. For studies of Xe polarization dynamics, shorter pulses (0.6125 ms) were used to sample the ^{129}Xe magnetization during SEOP; the cumulative effect of these pulses (1/min) was separately determined to be equivalent to an additional relaxation contribution to the apparent time constant governing SEOP (Γ, see Eq. (2.6)) of $\sim 3.9 \times 10^{-4}\ s^{-1}$ (c.f. typical range of Γ values measured ($\sim 2.7 \times 10^{-3}$–$1.6 \times 10^{-2}\ s^{-1}$); all Γ values were thus corrected for the effect of the rf pulses by subtracting this number from the results of all raw fits of the experimental data). All low-field experiments were performed without rf/af shielding, and the resulting (magnitude) NMR spectra were obtained with a significant noise plateau (~20–30 counts). Correspondingly, each dataset was obtained by averaging four identical runs following subtraction of the noise plateau, and then shifted in time (so that the polarization growth began at 0 s) and subsequently fit to $S(t) = a \cdot (1 - \exp(-\Gamma t))$ to extract Γ and the steady-state ^{129}Xe NMR signal intensity ($a = \xi \cdot [Xe]_{cell} \cdot P_{Rb} \cdot \gamma_{SE} \cdot \Gamma^{-1}$, where ξ is an instrument function that includes characteristics of the spectrometer and its configuration, and subsumes all other parameters not explicitly provided).

For high-field NMR measurements, the xenon may be efficiently collected following OP using a glass liquid-N_2-cooled condenser residing in a ~1500 G field provided by two permanent magnets (Indigo Inst.); alternatively, the cell contents can be simply expanded into an evacuated stopcock-sealed NMR tube. High-field ^{129}Xe NMR spectra were recorded at 9.39 T (110.58 MHz) using a Varian spectrometer. HP ^{129}Xe spectra were obtained with a single 1 μs rf pulse ($\alpha = 6.7°$); corresponding thermally polarized ^{129}Xe signals were obtained from the same sample following careful addition of sufficient O_2 gas to reduce the ^{129}Xe T_1 (to a few s) to permit signal averaging ($\alpha = 90°$; typical recycle delay = 20 s).

Note added in proof

Readers may also be interested in recent work from Sheffield investigating off-resonant Rb/129Xe SEOP with tunable high-power external-cavity-narrowed LDAs [51].

Acknowledgments

We thank Drs. B. Saam (Utah), G. Schrank (PNNL), and A. Coy (Magritek) for helpful conversations and correspondence; G. Moroz (SIUC) for expert machining; and the late K. Owens (UMSL) for glassblowing. B.M.G. is a Cottrell Scholar of Research Corporation. Work at SIUC is supported by NSF (CAREER CHE-03492550, DMR-0552800), Research Corporation, and SIU ORDA & MTC. M.J.B acknowledges the generous support of the School of Medical & Surgical Sciences, University of Nottingham and GE Healthcare-Amersham.

References

[1] B.M. Goodson, Nuclear magnetic resonance of laser-polarized noble gases in molecules, materials, and organisms, J. Magn. Reson. 155 (2002) 157–216.
[2] A. Bifone, A. Cherubini, Hyperpolarised xenon in biology, Prog. Nucl. Magn. Reson. Spectrosc. 42 (2003) 1–30.
[3] M.S. Albert, G.D. Cates, B. Driehuys, W. Happer, B. Saam, C.S. Springer, Nature 370 (1994) 199–201.
[4] J.P. Mugler, B. Driehuys, J.R. Brookeman, G.D. Cates, S.S. Berr, R.G. Bryant, T.M. Daniel, E.E. del Lange, J.H. Downs III, C.J. Erickson, W. Happer, D.P. Hinton, N.F. Kassel, T. Maier, C.D. Phillips, B.T. Saam, K.L. Sauer, M.E. Wagshul, Magn. Reson. Med. 37 (1997) 809–815.
[5] S.D. Swanson, M.S. Rosen, B.W. Agranoff, K.P. Coulter, R.C. Welsh, T.E. Chupp, Magn. Reson. Med. 38 (1997) 695–698.
[6] X.J. Chen, M.S. Chawla, L.W. Hedlund, H.E. Moller, J.R. MacFall, G.A. Johnson, Magn. Reson. Med. 39 (1998) 79–84.
[7] J.C. Leawoods, D.A. Yablonskiy, B. Saam, D.S. Gierada, M.S. Conradi, Hyperpolarized He-3 gas production and MR imaging of the lung, Concepts Magn. Reson. 13 (2001) 277–293.
[8] S. Patz, F.W. Hersman, I. Muradian, M. Hrovat, I.C. Ruset, S. Ketel, F. Jacobson, G. Topulos, H. Hatabu, J. Butler, Hyperpolarized ^{129}Xe MRI: a viable functional lung imaging modality?, Eur J. Radiol. 64 (2007) 335–344.
[9] D. Raftery, H. Long, T. Meersmann, P.J. Grandinetti, L. Reven, A. Pines, Phys. Rev. Lett. 66 (1991) 584–587.
[10] Y.-Q. Song, B.M. Goodson, R.E. Taylor, D.D. Laws, G. Navon, A. Pines, Selective enhancement of NMR signals for α-cyclodextrin with laser-polarized xenon, Angew. Chem., Int. Ed. Engl. 36 (1997) 2368–2370.
[11] D. Raftery, E. MacNamara, G. Fisher, C.V. Rice, J. Smith, J. Am. Chem. Soc. 119 (1997) 8746–8747.
[12] S.M. Rubin, M.M. Spence, B.M. Goodson, D. Wemmer, A. Pines, Proc. Natl. Acad. Sci. USA 97 (2000) 9472–9475.
[13] P. Sozzani, A. Comotti, R. Simonutti, T. Meersmann, J.W. Logan, A. Pines, Angew. Chem., Intl. Ed. Engl. 39 (2000) 2695–2698.
[14] I. Moudrakovski, S. Lang, C.I. Ratcliffe, B. Simard, G. Santyr, J.A. Ripmeester, Chemical shift imaging with continuously flowing hyperpolarized xenon for the characterization of materials, J. Magn. Reson 144 (2000) 372–377.
[15] C. Landon, P. Berthault, F. Vovelle, H. Desvaux, Protein Sci. 10 (2001) 762–770.
[16] J. Butler, R. Mair, D. Hoffmann, M. Hrovat, R. Rogers, G. Topulos, R.L. Walsworth, S. Patz, Measuring surface-area-to-volume ratios in soft porous materials using laser-polarized xenon interphase exchange nuclear magnetic resonance, J. Phys.: Condens. Matter 14 (2002) 297–304.
[17] K.F. Stupic, Z.I. Cleveland, G.E. Pavlovskaya, T. Meersmann, Quadrupolar relaxation of hyperpolarized krypton-83 as a probe for surfaces, Solid State Nucl. Magn. Reson. 29 (2006) 79–84.

[18] M.M. Spence, S.M. Rubin, I.E. Dimitrov, E.J. Ruiz, D. Wemmer, A. Pines, S. Qin Yao, F. Tian, P.G. Schultz, Functionalized xenon as a biosensor, Proc. Natl. Acad. Sci. USA 98 (2001) 10654–10657.
[19] L. Schroder, T. Lowery, C. Hilty, D. Wemmer, A. Pines, Molecular imaging using a targeted magnetic resonance hyperpolarized biosensor, Science 314 (2006) 446–449.
[20] B. Saam, N. Drukker, W. Happer, Chem. Phys. Lett. 263 (1996) 481–487.
[21] M.P. Augustine, A. Wong-Foy, J.L. Yarger, M. Tomaselli, A. Pines, D.M. TonThat, J. Clarke, Appl. Phys. Lett. 72 (1998) 1908–1910.
[22] J. Granwehr, E. Harel, S.-I. Han, S. Garcia, A. Pines, Time-of-flight flow imaging using NMR remote detection, Phys. Rev. Lett. 95 (2005).
[23] C.R. Bowers, H.W. Long, T. Pietrass, H.C. Gaede, A. Pines, Cross polarization from laser-polarized solid xenon to $13CO_2$ by low-field thermal mixing, Chem. Phys. Lett. 205 (1993) 168–170.
[24] G. Navon, Y.-Q. Song, T. Room, S. Appelt, R.E. Taylor, A. Pines, Enhancement of solution NMR and MRI with laser-polarized xenon, Science 271 (1996) 1848–1851.
[25] R.J. Fitzgerald, K.L. Sauer, W. Happer, Cross-relaxation in laser-polarized liquid xenon, Chem. Phys. Lett. 284 (1998) 87–92.
[26] A. Cherubini, G. Payne, M.O. Leach, A. Bifone, Hyperpolarising 13C for NMR studies using laser-polarised ^{129}Xe: SPINOe vs thermal mixing, Chem. Phys. Lett. 371 (2003) 640–644.
[27] T. Walker, W. Happer, Spin-exchange optical pumping of noble-gas nuclei, Rev. Mod. Phys. 69 (1997) 629–642.
[28] W. Happer, E. Miron, S. Schaefer, D. Schreiber, W.A.v. Wijngaarden, X. Zeng, Polarization of the nuclear spins of noble-gas atoms by spin exchange with optically pumped alkali-metal atoms, Phys. Rev. A 29 (1984) 3092–3110.
[29] G.D. Cates, R.J. Fitzgerald, A.S. Barton, P. Bogorad, M. Gatzke, N.R. Newbury, B. Saam, Rb-^{129}Xe spin-exchange rates due to binary and three-body collisions at high Xe pressures, Phys. Rev. A 45 (1992) 4631–4639.
[30] B. Driehuys, G.D. Cates, E. Miron, K. Sauer, D.K. Walter, W. Happer, High-volume production of laser-polarized Xe-129, Appl. Phys. Lett. 69 (1996) 1668–1670.
[31] M.E. Wagshul, T. Chupp, Phys. Rev. A 49 (1994) 3854.
[32] M.G. Mortuza, S. Anala, G.E. Pavlovskaya, T.J. Dieken, T. Meersmann, Spin-exchange optical pumping of high-density xenon-129, J. Chem. Phys. 118 (2003) 1581–1584.
[33] U. Ruth, T. Hof, J. Schmidt, D. Fick, H.J. Jansch, Production of nitrogen-free hyperpolarized ^{129}Xe gas, Appl. Phys. B 68 (1999) 93.
[34] A.L. Zook, B.B. Adhyaru, C.R. Bowers, High capacity production of >65% spin polarized xenon-^{129} for NMR spectroscopy and imaging, J. Magn. Reson. 159 (2002) 175–182.
[35] K. Knagge, J. Prange, D. Raftery, A continuously recirculating optical pumping apparatus for high xenon polarization and surface NMR studies, Chem. Phys. Lett. 397 (2004) 11–16.
[36] I.C. Ruset, S. Ketel, F.W. Hersman, Optical pumping system design for large production of hyperpolarized ^{129}Xe, Phys. Rev. Lett. 96 (2006) 053002.
[37] F.W. Hersman, I.C. Ruset, S. Ketel, I. Muradian, S.D. Covrig, J. Distelbrink, W. Porter, D. Watt, J. Ketel, J. Brackett, A. Hope, S. Patz, Large production system for hyperpolarized ^{129}Xe human lung imaging studies, Acad. Radiol. 15 (2008) 683–692.
[38] G. Schrank, Z. Ma, A. Schoeck, B. Saam, Characterization of a low-pressure high-capacity ^{129}Xe flow-through polarizer, Phys. Rev. A 80 (2009) 063424.
[39] P. Nikolaou, N. Whiting, N.A. Eschmann, K.E. Chaffee, M. Barlow, B.M. Goodson, Generation of laser-polarized xenon using fiber-coupled laser-diode arrays narrowed with integrated volume holographic gratings, J. Magn. Reson 197 (2009) 249–254.
[40] M.S. Rosen, T.E. Chupp, K.P. Coulter, R.C. Welsh, S.D. Swanson, Polarized ^{129}Xe optical pumping/spin exchange and delivery system for magnetic resonance spectroscopy and imaging studies, Rev. Sci. Instrum. 70 (1999) 1546–1552.
[41] B. Chann, I.A. Nelson, L.W. Anderson, B. Driehuys, T.G. Walker, ^{129}Xe-Xe molecular spin relaxation, Phys. Rev. Lett. 88 (2002).
[42] B.N. Berry-Pusey, B.C. Anger, G. Laicher, B. Saam, Nuclear spin relaxation of ^{129}Xe due to persistent xenon dimers, Phys. Rev. A 74 (2006).
[43] I. Saha, P. Nikolaou, N. Whiting, B.M. Goodson, Characterization of violet emission from Rb optical pumping cells used in laser-polarized xenon NMR experiments, Chem. Phys. Lett. 428 (2006) 268–276.
[44] M.V. Romalis, E. Miron, G.D. Cates, Pressure broadening of Rb D-1 and D-2 lines by He-3, He-4, N-2, and Xe: Line cores and near wings, Phys. Rev. A 56 (1997) 4569–4578.
[45] N. Whiting, P. Nikolaou, N. Eschmann, M.J. Barlow, B.M. Goodson, Effects of Laser Power, Linewidth, and Component Gas Densities on the Polarization of Xenon with Fixed-Frequency Volume Holographic Grating (VHG)-Narrowed Laser Diode Arrays, 49th Exptl., Nucl. Magn. Reson. Conf., Asilomar, CA, 2008.
[46] A. Fink, D. Baumer, E. Brunner, Production of hyperpolarized xenon in a static pump cell: numerical simulations and experiments, Phys. Rev. A 72 (2005) 053411.
[47] D.A. Steck, Rb 85 & 87 D-line Data, http://steck.us/alkalidata, rev. 2.1.2 (2009)
[48] C.V. Rice, D. Raftery, Rubidium-xenon spin exchange and relaxation rates measured at high pressure and high magnetic field, J. Chem. Phys. 117 (2002) 5632–5641.
[49] N. Whiting, P. Nikolaou, N. Eschmann, M. Barlow, and B.M. Goodson, Rb/Xe spin exchange optical pumping with tunable, high-power LDAs narrowed with on-chip volume holographic gratings, Opt. Express, in preparation.
[50] D.K. Walter, W.M. Griffith, W. Happer, Energy transport in high-density spin-exchange optical pumping cells, Phys. Rev. Lett. 86 (2001) 3264–3267.
[51] S.R. Parnell, M.H. Deppe, J. Parra-Robles, J.M. Wild, Enhancement of 129Xe polarization by off-resonant spin exchange optical pumping, J. Appl. Phys. 108 (2010) 064908.